The Dependence of Rossby Wave Breaking on the Vertical Structure of the Polar Vortex

Darryn W. Waugh*

Meteorology CRC, Monash University, Clayton, Victoria, Australia

David G. Dritschel[+]

Department of Mathematics, University of Warwick, Coventry, United Kingdom

ABSTRACT

The three-dimensional structure of wave propagation and breaking on the edge of polar vortices is examined using a multilayer quasigeostrophic model, with piecewise constant potential vorticity (PV) in each layer. The linear propagation of waves up the edge of a vortex is found to be sensitive to vertical variations in the vortex structure, with reduced propagation if the PV or area of the vortex increases with height; this reduction is dramatic for a cylindrical vortex with increasing PV. The characteristics of the nonlinear evolution and wave breaking is examined using high-resolution contour dynamics simulations and is also found to be sensitive to the vertical structure of the vortex. The amplitude of the forcing required for wave breaking to occur is larger for baroclinic vortices (with PV or area increasing with height) than for barotropic vortices. For cylindrical vortices with PV increasing with height the variation of wave breaking with forcing amplitude is qualitatively different from that of a barotropic vortex. Wave breaking occurs in the upper layers for only a limited, intermediate range of forcing amplitudes: there is no wave breaking in upper layers for weak forcing and for large forcing there is only wave breaking at the bottom of the vortex (i.e., the wave breaking is more vertically confined than for a barotropic vortex). For vortices with both PV and area increasing with height there is again a regime with wave breaking in the upper layers for weak amplitude forcing. However, the characteristics of the filaments produced by the wave breaking in upper layers is different from that in the barotropic case, with the filaments rolling up into a series of small vortices.

1. Introduction

Understanding the dynamics and transport across the edge of stratospheric polar vortices is important for understanding both ozone depletion and the large-scale circulation within the stratosphere (e.g., Schoeberl and Hartmann 1991; McIntyre 1992). The polar vortices are disturbed by planetary-scale Rossby waves that propagate up from the troposphere. The amplitude of these waves is such that they are strongly nonlinear, and this nonlinearity results in Rossby wave "breaking" (McIntyre and Palmer 1983, 1984). During this wave-breaking process, tongues of air are drawn from the vortex and transported into middle latitudes.

The first high-resolution view of this wave breaking was obtained by Juckes and McIntyre (1987), who performed simulations of a forced polar vortex in a hemispheric barotropic model. These simulations showed erosion of the vortex through the mixing of finescale filamentary structures into the midlatitude "surf zone." This evolution is consistent with that observed in potential vorticity (PV) fields from meteorological analyses (McIntyre and Palmer 1983, 1984) or in satellite measurements of long-lived tracers (Leovy et al. 1985), although the scale of features, such as the filaments surrounding the vortex and the gradients at the vortex edge, produced in the simulations are much smaller than those resolvable in the satellite-based data. Hence, the reality of these small-scale features cannot be verified by satellite data. However, more recent high-resolution in situ trace gas measurements and trajectory calculations driven by analyzed winds show finescale features very similar to those produced in model simulations

* Current affiliation: Department of Earth and Planetary Science, Johns Hopkins University, Baltimore, Maryland.

[+] Current affiliation: Mathematical Institute, University of St. Andrews, North Haugh, United Kingdom.

Corresponding author address: Dr. Darryn W. Waugh, Department of Earth and Planetary Sciences, Johns Hopkins University, 301 Olin Hall, 3400 N. Charles Street, Baltimore, MD 21218.
E-mail: waugh@jhu.edu

(e.g., Plumb et al. 1994; Waugh et al. 1994), suggesting that filamentary structures are produced during Rossby wave breaking in the stratosphere.

Numerous modeling studies have examined further the two-dimensional (latitude–longitude) structure of Rossby wave breaking at the edge of polar vortices (e.g., Juckes 1989; Salby et al. 1990a,b,c; Polvani and Plumb 1992; Waugh 1993; Yoden and Ishioka 1993; Norton 1994), but there have been very few studies that have examined the three-dimensional (3D) structure of Rossby wave breaking. Initial 3D nonlinear models of the stratospheric polar vortices lacked the horizontal resolution to resolve the finescale features produced during wave breaking (e.g., Butchart et al. 1982; Rose 1985), while subsequent studies using higher-resolution simulations that resolved, at least partially, these features generally focused on reproducing the observed features of the real atmosphere rather than the 3D structure of the wave breaking (e.g., Mahlman and Umscheid 1987; O'Neill and Pope 1988; Manney et al. 1994; Boville 1995; Beck 1996). Two exceptions are the studies of Haynes (1990) and Dritschel and Saravanan (1994).

Haynes (1990) examined the structure of the vortex and wave breaking in two idealized simulations of a forced stratospheric polar vortex in a high-resolution 3D (primitive equation) model and found qualitatively the same features as in the above single-layer simulations (i.e., wave breaking producing vortex erosion and filamentary structure surrounding the vortex). Dritschel and Saravanan (1994) (hereafter DS94) performed a series of simulations using a multilayer quasigeostrophic (QG) contour dynamics model. They examined the response of a barotropic vortex (represented as a patch of constant PV in each layer) to topographic forcing and again found behavior very similar to that in single-layer models. However, the vertical structure was qualitatively different for different forcing amplitudes: for weak forcing, wave breaking occurred only in the upper layers of the vortex, while for strong forcing there was vigorous wave breaking in the lower layers. They referred to the weak amplitude case as "remote" wave breaking and to the strong amplitude case as "local" wave breaking. (However, it is important to note that in the so-called local breaking regime there is still wave breaking in the upper layers, but this breaking is much weaker than that in the lower layers.) DS94 also noted that the filamentary structures produced during the wave breaking have a nearly barotropic structure.

As well as these studies using dynamical models, there have been several studies that have used transport calculations driven by analyzed winds to examine the 3D structure of filaments produced during wave-breaking events (e.g., Orsolini 1995; Orsolini et al. 1997; Schoeberl and Newman 1995; Mariotti et al. 1997). These studies have shown that the filaments observed in single-layer calculations (or horizontal aircraft transects) have vertical coherence and are in fact slices through vertically sloping sheets of anomalous air. Furthermore, Schoeberl and Newman (1995) showed evidence for the existence of the local and remote wave-breaking regimes noted by DS94.

In this study we extend the analysis of DS94 to consider baroclinic vortices, that is, vortices in which the PV and/or area varies with height. We use the same multilayer QG model as in DS94 and also consider only vortices that are represented by a single patch of constant PV in each layer. The dependence of both the linear and nonlinear response on the structure of the vortex is examined. In particular, we examine the effect of the initial vortex structure on the vertical wave propagation, the vertical extent of the wave breaking, and the structure of the vortex and filaments produced during these breaking events. The vortex erosion and structure of the vortex is quantified using the elliptical diagnostics of Waugh (1997) [see also Legras and Dritschel (1993) and Dritschel (1993)].

In section 2 we describe the QG contour dynamics model used in this study. The different initial vortices considered are then discussed in section 3. The linear dispersion relation and related linear propagation of vortex-edge waves are examined in section 4. Then in section 5 we examine, via high-resolution contour dynamics simulations, the nonlinear response, with particular attention paid to the vertical extent of wave breaking, the slope of the vortex core with height, and filamentary structure and stability. We conclude in section 6.

2. Model equations

The equations of motion for dissipative-free QG flow are

$$\frac{\mathrm{D}q}{\mathrm{D}t} \equiv \frac{\partial q}{\partial t} + \mathbf{u} \cdot \boldsymbol{\nabla}_h q = 0, \tag{1a}$$

$$\nabla_h^2 \psi + \frac{1}{\rho_0}\frac{\partial}{\partial z}\left(\rho_0 \frac{f_0^2}{N_0^2}\frac{\partial \psi}{\partial z}\right) = q, \tag{1b}$$

$$\frac{\partial \psi}{\partial z} = 0 \quad \text{at } z = 0 \quad \text{and} \quad z = D, \tag{1c}$$

$$u = -\frac{\partial \psi}{\partial y} \quad \text{and} \quad v = \frac{\partial \psi}{\partial x}, \tag{1d}$$

where $q(x, y, z, t)$ is the PV, ψ the geostrophic streamfunction, $\mathbf{u} = (u, v)$ the geostrophic velocity, $\boldsymbol{\nabla}_h$ the horizontal Laplacian operator, ρ_0 the density, D the domain height, f_0 the Coriolis parameter, and N_0 the Brunt–Väisälä frequency. Following DS94, the streamfunction ψ can be written as

$$\psi(\mathbf{x}, t) = \iiint d\mathbf{x}' \rho_0(z') G(\mathbf{x}'; \mathbf{x}) q(\mathbf{x}', t), \tag{2a}$$

where

$$G(\mathbf{x}'; \mathbf{x}) = -\frac{1}{2\pi} \sum_{n=0}^{\infty} \chi_n(z')\chi_n(z)K_0(\gamma_n r), \quad (2b)$$

$r^2 = x^2 + y^2$, K_0 is the modified Bessel function of zero order, $\chi_n(z)$ is the vertical structure function, and γ_n the internal radius of deformation of the nth mode. Here $\chi_n(z)$ and γ_n are the eigenvectors and eigenvalues of

$$\frac{d}{dz}\left(\rho_0 \frac{f_0^2}{N_0^2} \frac{d\chi_n}{dz}\right) + \gamma_n^2 \rho_0 \chi_n = 0 \quad \text{with} \quad \frac{d\chi_n}{dz} = 0 \quad \text{at } z = 0, D.$$
$$(3)$$

Here we consider the ''compressible'' case ($\rho_0 = \hat{\rho}_0 e^{-z/H}$; f_0 and N_0 constant), which is the relevant case for stratospheric flow. Following Dritschel and de la Torre Juárez (1996), we have (for $n > 0$)

$$\chi_n(z) = \rho_0^{-1/2}(z)\overline{\chi}_n(z),$$

$$\overline{\chi}_n(z) = \hat{\chi}_n\left[\sin\left(\frac{n\pi z}{D}\right) - \frac{2n\pi H}{D}\cos\left(\frac{n\pi z}{D}\right)\right], \quad (4a)$$

and

$$\gamma_n^2 = \frac{f_0^2}{N_0^2}\left[\left(\frac{n\pi}{D}\right)^2 + \frac{1}{4H^2}\right], \quad (4b)$$

where the functions $\overline{\chi}_n$ are orthonormal, $\hat{\chi}_n$ are constants; the first mode χ_0 is independent of z and $\gamma_0 = 0$. Note that in the Boussinesq case (ρ_0 constant) the structure functions are $\chi_n(z) = \hat{\chi}_n \cos(n\pi z/D)$ and $\gamma_n = n\pi f_0/(N_0 D)$.

We now consider the discretized version (the domain $z = 0$ to D is divided into L layers of equal depth, $\Delta z = D/L$) of the case where the PV is piecewise uniform at every height z. The velocity at each midlayer $z_j = (j - \frac{1}{2})\Delta z$ is then (see DS94 for details)

$$\mathbf{u}_j = -\sum_{\ell=1}^{L}\sum_{k=1}^{n_\ell} \rho_\ell \tilde{q}_{\ell k} \oint_{C_\ell^k} G_{j\ell}(r)(dx', dy'), \quad (5a)$$

where

$$G_{j\ell}(r) = -\frac{1}{2\pi}\sum_{n=0}^{L-1} \chi_{jn}\chi_{\ell n}K_0(\gamma_n r), \quad (5b)$$

$\tilde{q}_{\ell k}$ is the PV discontinuity on contour C_ℓ^k in layer ℓ, and $\chi_n = \{\chi_{0n}, \chi_{1n}, \ldots, \chi_{L-1n}\}$ is the discretized version of (4a), that is, $\chi_{\ell n} = \chi_n(z_\ell)$.

3. Initial conditions

In this study we consider the case where there is a single contour of PV discontinuity in each layer, and the contour is initially circular. Both the potential vorticity q inside the contour and the initial area A of the contour can vary with height.

We restrict our attention to vortices in which the vertical variations of q and A are given by the first baroclinic structure function $\chi_1(z)$, that is,
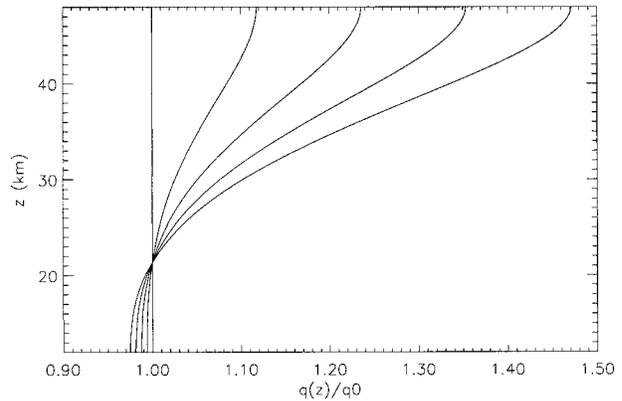
$$q(z) = \hat{q}_0 + \hat{q}_1\chi_1(z) \quad (6a)$$

Fig. 1. Vertical variation of $q/\hat{q}_0$ as given by Eq. (8a) for $\hat{q}_1/f_0 = 0, 0.025, 0.05, 0.075,$ and 1.0 (with $\hat{q}_0 = 0.8\, f_0$).

and

$$A(z) = \hat{A}_0 + \hat{A}_1\chi_1(z). \quad (6b)$$

As $\chi_1(z)$, given by (4), is monotonically increasing, $q(z)$ and $A(z)$ increase with z for positive $\hat{q}_1$ and $\hat{A}_1$. Also, as χ_1 is only weakly dependent on z for small z, the vortices are nearly barotropic in the lower part of the domain. This can be seen in Fig. 1, which shows $q(z)/\hat{q}_0$ [or equivalently $A(z)/\hat{A}_0$] for several values of $\hat{q}_1(\hat{A}_1)$.

The initial vortex is further constrained so that it has the same total circulation Γ as a barotropic vortex with $q = \hat{q}_b$ and $A = \hat{A}_b$, that is,

$$\Gamma \equiv \int_0^D dz\, \rho_0(z)q(z)\alpha(z) = \hat{q}_b\hat{A}_b \int_0^D dz\, \rho_0(z) \quad (7)$$

[$\alpha(z)$ is the area enclosed by the contour]. If $A = \hat{A}_b$, then (7) is satisfied for $\hat{q}_0 = \hat{q}_b$ and arbitrary $\hat{q}_1$ [this follows from the fact that $\int_0^D dz\, \rho_0(z)\chi_1(z) = 0$]. Similarly, (7) is satisfied for $q = \hat{q}_b$, $\hat{A}_0 = \hat{A}_b$, and arbitrary $\hat{A}_1$.

Considering only vortices with the same total circulation and weak vertical variations in the lowest layers enables a clean analysis of the dependence of wave propagation and breaking on the vertical structure of the vortex. For a given disturbance amplitude the evolution in the lowest layers will be very similar for all vortices satisfying (6) and (7), and differences in the upper layers will be because of changes in the vertical structure of the vortices (rather than, say, changes in the amplitude of the forcing relative to the vortex circulation).

To examine the relative effects of vertical variations in q and A we consider three different families of vortices: family $\mathcal{A}$ in which A is constant (independent of z), family $\mathcal{B}$ in which q is constant, and family $\mathcal{C}$ in which both A and q vary with z. Specifically, the vortex area and PV within each family are

TABLE 1. Parameter values of vortices shown in paper; see text for definitions of parameters.

Vortex	$\hat{q}_0/f_0$	$\hat{q}_1/f_0$	$\hat{A}_0/\pi L_R^2$	$\hat{A}_1/\pi L_R^2$	u_B (m s^{-1})	u_T (m s^{-1})	Family
V1	0.8	0.0	3.0	0.0	58	58	$\mathcal{A}$, $\mathcal{B}$
V2	0.8	0.05	3.0	0.0	56	81	$\mathcal{A}$
V3	0.8	0.10	3.0	0.0	55	105	$\mathcal{A}$, $\mathcal{C}1$
V4	0.8	0.0	3.0	1.0	59	55	$\mathcal{B}$
V5	0.8	0.0	3.0	3.0	58	43	$\mathcal{B}$
V6	0.794	0.10	3.0	0.5	56	105	$\mathcal{C}1$
V7	0.786	0.11	3.0	1.0	56	106	$\mathcal{C}1$

$(\mathcal{A})$ $\hat{A}_0 = \hat{A}_b$, $\hat{A}_1 = 0$, $\hat{q}_0 = \hat{q}_b$,   and $\hat{q}_1 \geqq 0$;

$(\mathcal{B})$ $\hat{A}_0 = \hat{A}_b$, $\hat{A}_1 \geqq 0$, $\hat{q}_0 = \hat{q}_b$,   and $\hat{q}_1 = 0$;

$(\mathcal{C})$ $\hat{A}_0 = \hat{A}_b$, $\hat{A}_1 \geqq 0$, $\hat{q}_0 \leqq \hat{q}_b$,   and $\hat{q}_1 \geqq 0$.

Family $\mathcal{C}$ can be divided into subfamilies within which all vortices have approximately the same (vertically varying) velocity at the vortex edge; that is, within a subfamily the velocity at the vortex edge in the bottom layer u_B and in the top layer u_T are approximately the same for all vortices. Here we consider one such subfamily ($\mathcal{C}1$): the subfamily with $u_B \approx 56$ m s^{-1} and $u_T \approx 106$ m s^{-1}. (Note that there are many possible partitions of family $\mathcal{C}$, and another physically meaningful partition could be to form subfamilies with the same angular velocity at the vortex edge.)

In the barotropic vortex case, $q = \hat{q}_b$ and $A = \hat{A}_b \equiv \pi \hat{R}_b^2$, we use the same parameters as DS94, that is, density-scale height $H = 6.14$ km, vortex height $D = 5.86H = 36$ km, reference Rossby radius $L_R = 902$ km, vortex radius $\hat{R}_b = 3L_R$, zero-wind radius $r_z = 6L_R$, PV inside the vortex $\hat{q}_b^i = 1.3f_0$, and PV outside the vortex $\hat{q}_b^o = 0.9f_0$ (hence $\tilde{q}_b = 0.4f_0$). With this setting the maximum wind speed, which occurs at $\hat{R}_b \approx 2700$ km (latitude $\approx 65°$), is around 60 m s^{-1}, and the zero-wind line occurs at around $r_z \approx 5400$ km (latitude $\approx 40°$); this flow is the same as in the single-layer simulations of Polvani and Plumb (1992).

Many simulations have been performed for vortices within each of the three families ($\mathcal{A}$–$\mathcal{C}$) but results are shown for only two or three vortices from each family. These vortices are listed in Table 1, and the corresponding flow fields are shown in Fig. 2 (the thick dashed curve corresponds to the vortex edge and the thick solid curve to the zero-wind line). The top row corresponds to vortices in family $\mathcal{A}$, the middle row to family $\mathcal{B}$, and the bottom row to subfamily $\mathcal{C}1$. As discussed above, the flow in the lower part of domain is very similar for all vortices and is approximately that of the barotropic vortex. However, there are large differences in the flow in the upper half of the domain.

For vortices in family $\mathcal{A}$ the maximum wind speed increases with height (for $\hat{q}_1 > 0$) and occurs at the same location (vortex edge, $\hat{R}_b$); see Figs. 2a,b. For increased $\hat{q}_1$ there is an increase in the difference between the maximum wind speed at the top and bottom of the vortex (the velocity at the bottom decreases slight-ly, while the velocity at the top increases substantially). Note that away from the vortex edge the flow is relatively unchanged from that of the barotropic vortex (i.e., the contours are nearly vertical).

The variation of the flow for vortices in family $\mathcal{B}$ is very different from that for those vortices in family $\mathcal{A}$; see Figs. 2c,d. For increasing $\hat{A}_1$ the maximum velocity at the top of the vortex decreases, but the velocity difference is small even when there is a large variation in $A(z)$. For example, with $\hat{A}_1 = 3\pi L_R^2$ (Fig. 2d) the radius of the vortex increases from 2500 to 4700 km, but the maximum velocity only decreases from 58 to 43 m s^{-1} (note, however, that the angular velocity decreases from 2.3×10^{-5} to 0.9×10^{-5} s^{-1}).

By definition, the initial flow for all vortices in the subfamily $\mathcal{C}1$ is very similar; see Figs. 2b,e,f. (Note again that there a change in the angular velocity, with the value at the top of the vortex decreasing from 3.8×10^{-5} to 3.0×10^{-5} s^{-1} for the three vortices shown.) As $\hat{A}_1$ increases, the size of the vortex in the upper half of the domain increases but the maximum wind speed and location of zero-wind radius is relatively unchanged. Note that, as the location of the zero-wind line does not vary significantly and the radius of the vortex edge increases, there is a decrease with height in the separation of the vortex edge and the zero-wind line.

The vertical variations in location and magnitude of maximum velocity in the above idealized vortices are comparable with that of the observed stratospheric polar vortices. For example, climatological observations of the Antarctic polar jet (e.g., Randel 1992) show that in midwinter (June–July) the maximum wind speed increases from around 40 m s^{-1} at 20 km to around 95 m s^{-1} at 50 km, and the latitude of jet maximum varies from 60°S ($\approx$3300 km) at 20 km to 45°S ($\approx$4800 km) at 50 km. In late winter to early spring (September–October) the jet is more vertically aligned (around 60°S) and the maximum wind speed is weaker and located in the middle stratosphere, while in late spring (November) the vortex has broken down in the upper stratosphere and the jet weakens and tilts poleward with height. The structure and seasonal evolution of the Arctic vortex is similar to the Antarctic jet, although the jet speed and vertical variation are much weaker for the Arctic polar vortex. Comparing the idealized vortices discussed above with the observed vortices, the flow field shown in Fig. 2f is probably
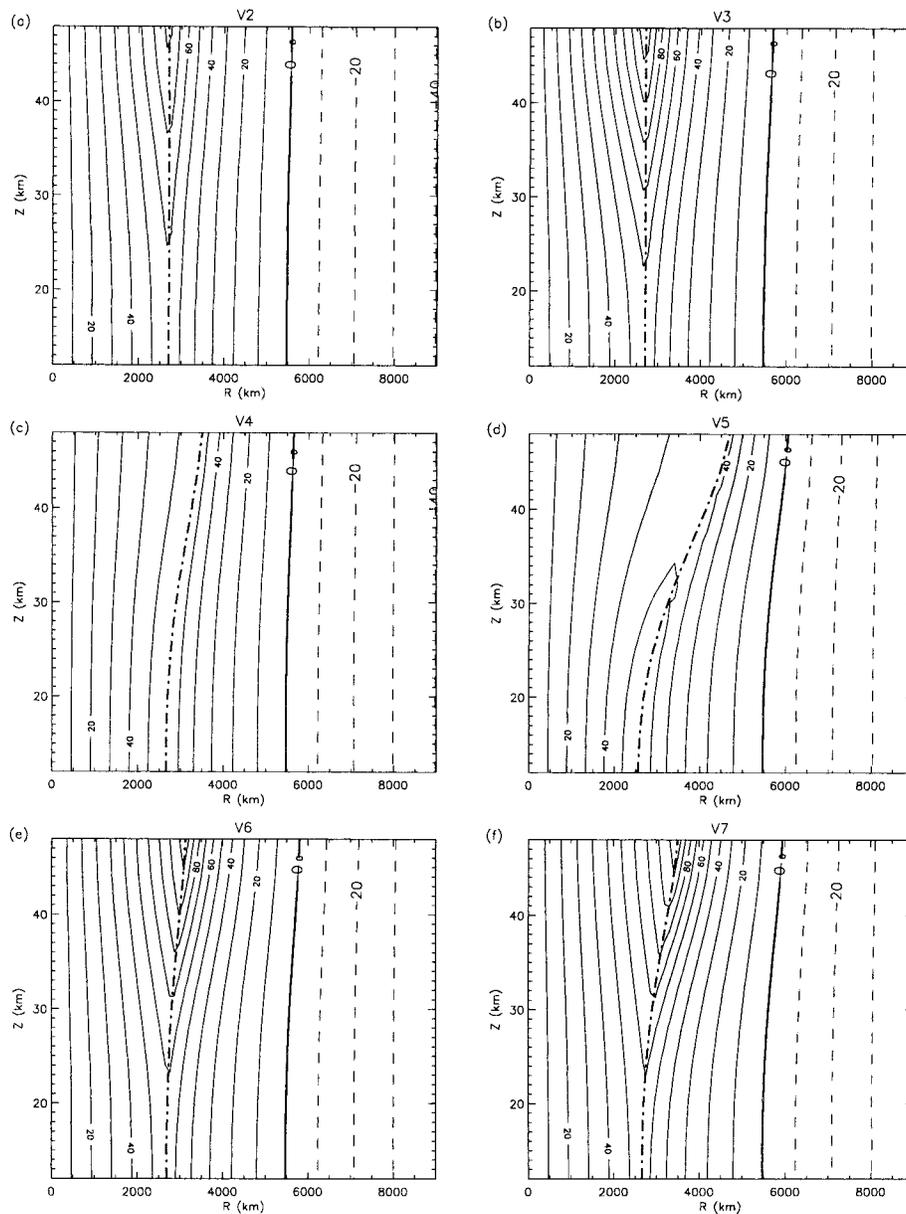
FIG. 2. Altitude–radius plots of the initial velocity for vortices (a) V2, (b) V3, (c) V4, (d) V5, (e) V6, and (f) V7 (see Table 1 for details). The thick solid curve is the zero-wind line, and the thick dash–dotted curve is the vortex radius. Contour interval is 10 m s^{-1} and negative values are shown as dashed curves.

the most realistic for early winter and midwinter conditions, while the barotropic vortex is probably the most realistic for late winter (at least for the Antarctic vortex). Note that as the size of the Antarctic vortex generally decreases with height in late spring (e.g., Mechoso 1990; Lahoz et al. 1996), vortices with q or A decreasing with height may be more realistic representations of the stratospheric vortices during late spring; however, due to space constraints, we do not consider these vortices here.

4. Linear response

We examine in this section the linear propagation of waves on the edge of the vortices described in the previous section. The dispersion relation, and hence the linear propagation of waves, for the L-layer QG system is determined in the same manner as the stability analysis of single-layer PV strips by Dritschel (1989) and Waugh and Dritschel (1991).

a. Linear dispersion relation

We consider azimuthal wavenumber m disturbances to each contour; that is, the contour position at layer j is $r_j(\theta, t) = R_j + \eta_j(\theta, t)$, where

$$\eta_j(\theta, t) = \hat{\eta}_j e^{i(m\theta - \sigma t)}. \qquad (8)$$

Let $\mathbf{u}_j = (u_r, u_\theta)_j = \overline{\mathbf{u}}_j + \mathbf{u}'_j + O(\eta^2)$ and $\mathbf{u}'_j = \hat{\mathbf{u}}_j e^{i(m\theta - \sigma t)}$; then from (5) we have $\overline{u}_{rj} = 0$:

$$\overline{u}_{\theta j} = -\sum_{\ell=1}^{L} r X_{j\ell}^1(R_\ell, r), \qquad (9a)$$

and

$$\hat{u}_{rj} \equiv im \sum_{\ell=1}^{L} X_{j\ell}^m(R_\ell, r), \qquad (9b)$$

where

$$X_{j\ell}^m(r_1, r_2) \equiv \rho_\ell q_\ell \frac{r_1}{r_2} \sum_{n=0}^{L-1} \chi_{jn} \chi_{\ell n} \begin{cases} K_m(\gamma_n r_1) I_m(\gamma_n r_2), & (r_1 > r_2) \\ I_m(\gamma_n r_1) K_m(\gamma_n r_2), & (r_1 < r_2), \end{cases}$$

and I_m and K_m are the modified Bessel functions of the mth order.

Using the linearized kinematic condition

$$\left(\frac{\partial}{\partial t} + \Omega \frac{\partial}{\partial \theta}\right)\eta = u'_r,$$

where $\Omega \equiv \overline{u}_\theta / r$, in each layer j, together with Eqs. (8) and (9), we obtain the L coupled equations

$$(c - \overline{\Omega}_j)\hat{\eta}_j + \sum_{\ell=1}^{L} X_{j\ell}^m \hat{\eta}_\ell = 0, \qquad (10)$$

where

$$\overline{\Omega}_j = \sum_{\ell=1}^{L} X_{j\ell}^1$$

and $c = \sigma/m$. Solvability of (10) requires determining c as an eigenvalue of an $L \times L$ eigensystem for each zonal wavenumber m. In general there are L solutions for c (eigenvalues c_ℓ, $\ell = 1, 2, \ldots, L$), each with a distinct vertical structure [eigenvectors $\mathbf{e}_\ell = (e_{1\ell}, e_\ell, \ldots, e_{L\ell})$].

The vertical structure of an initial disturbance can be expressed as a linear combination of these eigenvectors, that is,

$$\hat{\eta}_j = \sum_{\ell=1}^{L} \alpha_\ell e_{j\ell}.$$

Then, from (8), the linear evolution of this disturbance is

$$\eta_j(\theta, t) = \sum_{\ell=1}^{L} \alpha_\ell e_{j\ell} e^{im(\theta - c_\ell t)}, \qquad (11)$$

where c_ℓ and $\mathbf{e}_\ell$ are the eigenvalues and eigenvectors of (10). In other words, given the eigenvalues and eigenvectors of (10), the linear evolution of any wave-m disturbance is given by Eq. (11).

Note that if any of the c_l are complex, then exponential growth occurs and the vortex is linearly unstable. However, the PV profiles chosen here exclude this possibility, and, in fact, all are stable in a nonlinear sense (Dritschel 1988).

For the case of a barotropic vortex ($q_j = \hat{q}_b$ and $R_j = \hat{R}_b$ for all j) the dispersion relationship can be greatly simplified. Rewriting (10) in terms of the amplitude of the vertical modes rather than the disturbance to each contour, the equations become uncoupled and the phase speed of the nth vertical mode is given by

$$c_n = \hat{q}_b \left[\frac{1}{2} - K_m(\gamma_n \hat{R}_b) I_m(\gamma_n \hat{R}_b)\right].$$

Although we have considered only a single contour per layer, the above analysis can easily be extended to consider multiple contours in each layer and hence can be used to examine wave propagation (and stability) for more smoothly varying PV distributions. Furthermore, this analysis could also be used to examine the propagation of waves on the tropopause (e.g., Saravanan 1994).

Using the above analysis, we next examine the linear propagation of waves up the edge of vortices within each family. The wave propagation is quantified by calculating the wave activity W of the flow. The wave activity quantifies the mean-square amplitude of disturbances relative to the (circular) basic state (Dritschel 1988), and, in the absence of forcing, it is conserved. The wave activity for the L-layer QG system is defined as (see appendix B of DS94)

$$W = \int_0^D \hat{W}(z) \, dz = \int_0^D \rho_0(z) \tilde{q}(z) \hat{w}(z) \, dz,$$

where

$$\hat{w}(z) = \frac{1}{4}\left(\oint_{C(z)} (x^2 + y^2)(x \, dy - y \, dx) - \frac{2}{\pi}\alpha^2(z)\right),$$

and α is the area of the contour. Here $\hat{W}$ is the wave activity density at given z and includes the effect of vertical variations in density and PV, whereas $\hat{w}$ does not include these effects and is dependent only on the mean-square displacement of the contour, at each level, from circular symmetry.

b. Results

We examine here the response to an initial wavenumber m disturbance applied only to the bottom layer of the vortex, that is, $\hat{\eta}_j = 0$ for $j > 1$. Note that this is not the most appropriate initial disturbance when considering the linear response to the topographic forcing considered in the next section: as discussed in section 6 of DS94, the flow induced by this topography has a deep vertical structure, and so it would be more appropriate to consider an initial disturbance with some ver-
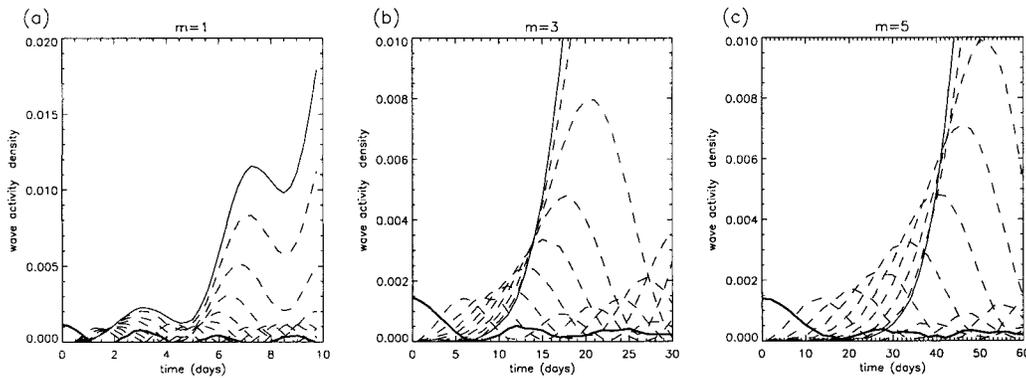
FIG. 3. Temporal variation of $\hat{w}$ for a barotropic vortex with an initial wave-m disturbance; (a) $m = 1$, (b) $m =$ 3, (c) $m = 5$. The thick solid curve is the bottom layer, the thin solid curve the top layer, and dashed curves are the intermediate layers.

tical extent. Also, a steady forcing, rather than a single initial pulse, is considered in the next section. However, we consider here a localized initial disturbance as we wish to examine the general propagation characteristics of linear waves on the edge of the vortex (and not just the linear version of the nonlinear simulations discussed in the next section).

Figure 3 shows the temporal evolution of $\hat{w}$ in each layer for a 10-layer barotropic vortex with initial $m =$ 1, 3, and 5 disturbances (the thick solid curve is the bottom layer and the thin solid curve the top layer). For all three wavenumbers, there is a general increase in $\hat{w}$ with z, and the values in the upper layers are much larger than in the bottom layers. This implies that the departures away from circular symmetry are largest in the upper layer. There is a large difference in the temporal variation of $\hat{w}$ for the different wavenumbers (note the different timescales shown in the three plots in Fig. 3), with the growth rate of $\hat{w}$ in upper layers decreasing and the time lag between maxima in upper and lower layers increasing for larger m. Note that because of the rapid decrease in density with height, the vertical variation of the wave activity density $\hat{W}$ is the opposite to that of $\hat{w}$ (i.e., largest values of $\hat{W}$ are in the bottom layers), and the total wave activity W is dominated by the wave activity in the bottom layers (see Fig. 9 of DS94).

Note that the initial disturbance of a single pulse to the bottom layer projects onto *all* vertical modes, and the vertical waves are highly dispersive. Hence, the initial pulse does not simply propagate up the vortex as a single packet (i.e., there is not a single peak in wave activity at each level of the vortex). Also, as there is no dissipation, the waves will reflect off the upper boundary, and the reflection of the fast waves produces the oscillatory response in Fig. 3.

The temporal evolution of $\hat{w}$ in the top layer for several vortices within families $\mathcal{A}$ (left column), $\mathcal{B}$ (middle column), and $\mathcal{C}1$ (right column), for $m = 1$ (top) and 3 (bottom), is shown in Fig. 4 (note different time-scales). These plots show that the wave activity in the upper layer varies dramatically with changes to the vortex structure, particular for $m = 3$.

Consider first family $\mathcal{A}$ (fixed A, variable q). As q_1 increases (i.e., increasing vertical PV gradient) there is only a small change in the time for vertical propagation (i.e., the maxima in wave activity occur at roughly the same time) but the amplitude of the waves decrease. The decrease in amplitude in the upper layers with increasing $\hat{q}_1$ becomes more pronounced with m [the decrease for $m = 5$ is even larger than for $m = 3$; e.g., for $\hat{q}_1 = 0.05 f_0$ (vortex V2 in Table 1) the value of $\hat{w}$ in the top layer when $m = 5$ is three orders of magnitude less than for the barotropic vortex]. Note that for large $\hat{q}_1$, $\hat{w}$ in the top level for $m = 3$ is less than that in the bottom layer (in contrast to the barotropic case; see Fig. 3), and hence the upper layer is less disturbed than the lower layers. These results indicate that an increase in the vertical gradient of PV of a cylindrical vortex inhibits the vertical propagation of waves on the vortex, and the effect is larger for smaller-scale waves.

For vortices with increasing A but fixed q (family $\mathcal{B}$), both the timing and amplitude of vertical propagation differ from the barotropic vortex. For an $m = 1$ disturbance, as $\hat{A}_1$ increases the vertical propagation is slower; that is, the maximum in $\hat{w}$ occurs later for larger $\hat{A}_1$. There is also a change in the amplitude in the upper layer, but whether the amplitude increases or decreases varies between local maxima. The amplitude of the first maximum (around 3–5 days) increases with $\hat{A}_1$, but this is not the case for later maxima (e.g., the second maximum for $\hat{A}_1 = 3\pi L_R^2$ is less than 0.1, not shown). However, the change in amplitude is much smaller than for increasing q (family $\mathcal{A}$), while, for all the vortices considered, the amplitude of $\hat{w}$ in the upper layer for $m = 1$ is similar. This, however, is not the case for $m = 3$. The magnitude of $\hat{w}$ in the upper layer is much less than for the barotropic vortex and, as in the case of increasing q, $\hat{w}$ in the top layer is less than $\hat{w}$ in the bottom layer
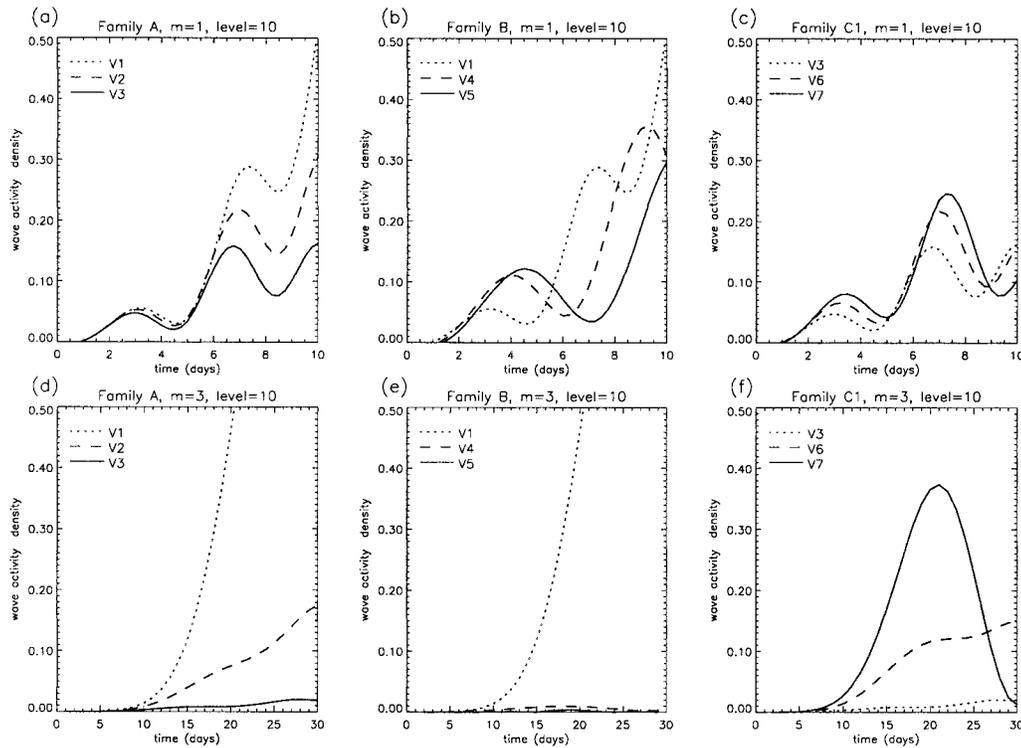
FIG. 4. Temporal evolution of $\hat{w}$ in the top layer for several vortices within families (a), (d) $\mathcal{A}$; (b), (e) $\mathcal{B}$; and (c), (f) $\mathcal{C}1$, for $m = 1$ (top) and 3 (bottom) disturbances. Vortices shown in each family are given in the legends.

for large $\hat{A}_1$. Hence, the vertical propagation of $m = 3$ waves is greatly inhibited by increasing A (for fixed q).

For vortices with approximately the same edge velocity but varying q and A (i.e., family $\mathcal{C}1$) there is only a small variation in $\hat{w}$ in the top layer when $m = 1$ but there is a large variation when $m = 3$. In particular, comparing with family $\mathcal{B}$ we see that the variation in $\hat{w}$ (in layer 10) for increasing A and q is very different than for increasing A alone. In the latter case there is a dramatic decrease in vertical propagation with increasing $\hat{A}_1$, but this is not the case when both A and q vary (e.g., vortex V7).

The above results show that the vertical propagation of waves is sensitive to the vortex structure (with increased sensitivity for smaller-scale waves). The exact details of the propagation depend on both q and A, and there does not appear to be a simple rule, although, in general, increasing q or A inhibits vertical propagation.

The linear results can be used to obtain a first-order estimate for the forcing amplitude necessary to bring about a nonlinear response (i.e., wave breaking). If we assume that wave breaking occurs when $\hat{w}$ exceeds some critical value, then Fig. 4 indicates that the amplitude of an initial disturbance required to produce wave breaking will vary for different initial vortices. For example, for an $m = 1$ disturbance, the critical amplitude (for wave breaking within 12 days) for vortices V3 and V7 would be around 3 and 2.5 times that of vortex V1,

respectively (as the maximum $\hat{w}$ for V1 is 3.0 and 2.5 times that of V3 and V7). Nonlinear (contour dynamics) numerical simulations confirm that the actual critical amplitude required agrees well with these linear estimates (not shown). Note that for $m = 3$ disturbances, the difference in critical amplitudes is much larger. As wave breaking (filamentation) occurs when contours cross stagnation points (e.g., Polvani and Plumb 1992), the critical amplitude for wave breaking may not only depend on the disturbance amplitude but also on the initial distance between the vortex edge and the zero-wind line. For smaller distances, we may expect wave breaking for smaller disturbance amplitudes.

5. Nonlinear response

a. Contour dynamics calculations

We now consider the nonlinear evolution of the vortices. The contour dynamics numerical method is used to solve Eq. (5) and simulate the nonlinear evolution. The multilayer QG contour surgery algorithm is that used in DS94. We use the spatial resolution parameter $\mu = 0.1$ (which corresponds to initially 72 nodes per contour) and surgery parameter $\delta = \mu^2/8$ (which corresponds to a filament-removal scale of around 3 km).

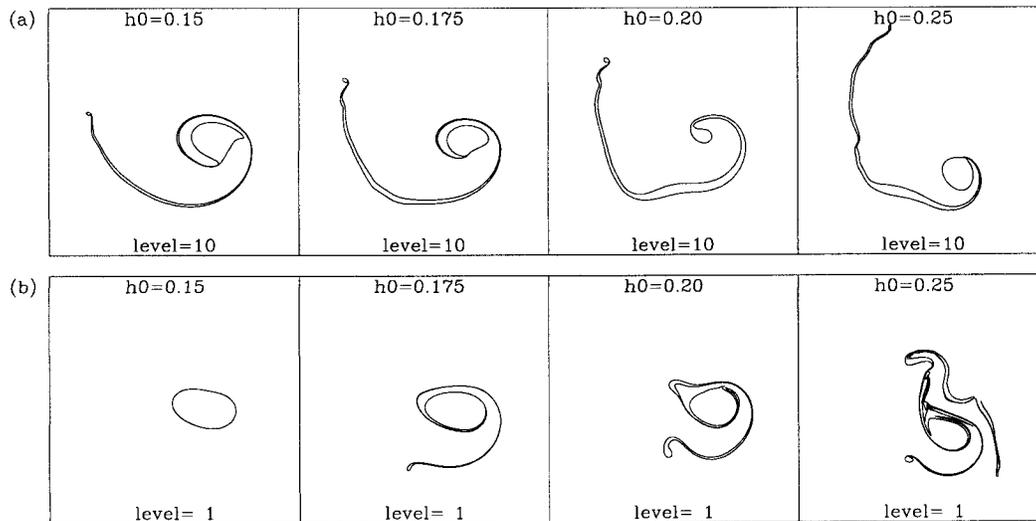As in DS94, the vortices are forced with bottom topography given by

FIG. 5. PV contours at $t = 12$ on (a) layer 10 (upper) and (b) layer 1 (lower) for barotropic vortex (V1) with $h_0 = 0.15$, 0.175, 0.20, and 0.25 (left to right).

$$h(x, y) = h_0 H J_1(1.6r/\hat{R}_b) \mathcal{R}(r) \cos\theta,$$

where h_0 is the nondimensional amplitude, J_1 is the first-order Bessel function, and

$$\mathcal{R}(r) = \begin{cases} 1, & r < 5, \\ \cos(\pi(r - 5)/5) & 5 \geq r \geq 7.5, \\ 0, & r > 7.5. \end{cases}$$

This form of h is very similar to that used in the single-layer planar simulations of Polvani and Plumb (1992) (and also Waugh 1993). The topography is switched on at $t = 0$ and is constant with time.

An extensive series of 10-layer simulations have been performed for several vortices within each family and a range of forcing amplitudes ($0.05 \leq h_0 \leq 0.25$). We have repeated several calculations using 20 layers and the results discussed below hold whether 10 or 20 layers are used (e.g., compare the 10-layer simulations for a barotropic vortex shown below with the 20-layer simulations shown in DS94).

As the contour dynamics simulations performed do not contain explicit diffusion or diabatic processes (the only nonconservative effects are those caused by the surgery algorithm, which operates on horizontal scales around 3 km), we restrict our integration period to 12 days. This is about the timescale when nonconservative processes are thought to start playing a role in the real stratosphere (e.g., Haynes and Ward 1993; Waugh et al. 1997; Haynes and Anglade 1997).

Figure 5 shows the PV on the bottom and top layers of the barotropic vortex after 12 days for several values of h_0 ($h_0 = 0.15$, 0.175, 0.20, 0.25; left to right). These simulations are the 10-layer versions of the (case $\mathcal{C}$) 20-layer simulations of DS94, and they produce very similar results (cf. Fig. 4 of DS94). As the forcing amplitude increases, the disruption to the vortex increases, partic-

ularly at the bottom of the vortex. For small amplitude ($h_0 \lesssim 0.15$) there is no wave breaking or filamentation in the bottom layer (at this resolution; using a smaller μ may produce some small filamentation for $h_0 \approx 0.15$), but wave breaking (producing a tongue of PV) occurs in the upper layer. This is the "remote breaking" regime discussed by DS94. On the other hand, for large amplitude ($h_0 > 0.2$) the vortex is very distorted in the lower layers. This is the "local breaking" regime of DS94. As discussed in section 1 there is still wave breaking in upper layers in the local breaking regime, but this wave breaking is much weaker than in the lower layers. Note that for intermediate amplitude forcing ($h_0 \approx 0.175$) there is wave breaking with similar characteristics throughout the height of the vortex, and this breaking cannot be classified into either the remote or local breaking regime.

For all h_0, the wave breaking near the top of the vortex occurs first in the top layer then moves down the vortex, and hence there is a possibility that this wave breaking is artificially caused by the top of the model. However, 20-layer simulations have been performed with the height of the vortex doubled, and the evolution in the lower half of this vortex (which corresponds to the domain of the 10-layer simulations) is almost identical to that in the above 10-layer simulations (not shown). This indicates that the wave breaking in the upper layers of the 10-layer simulations is not an artifact of the upper boundary. [Fyfe and Wang (1997) have recently examined the effect of the upper-boundary condition in multilayer contour dynamics simulations, and although they found that this boundary condition influenced the results in constant density (Boussinesq) simulations, there was not a significant effect for simulations with exponentially decreasing density as considered here.]

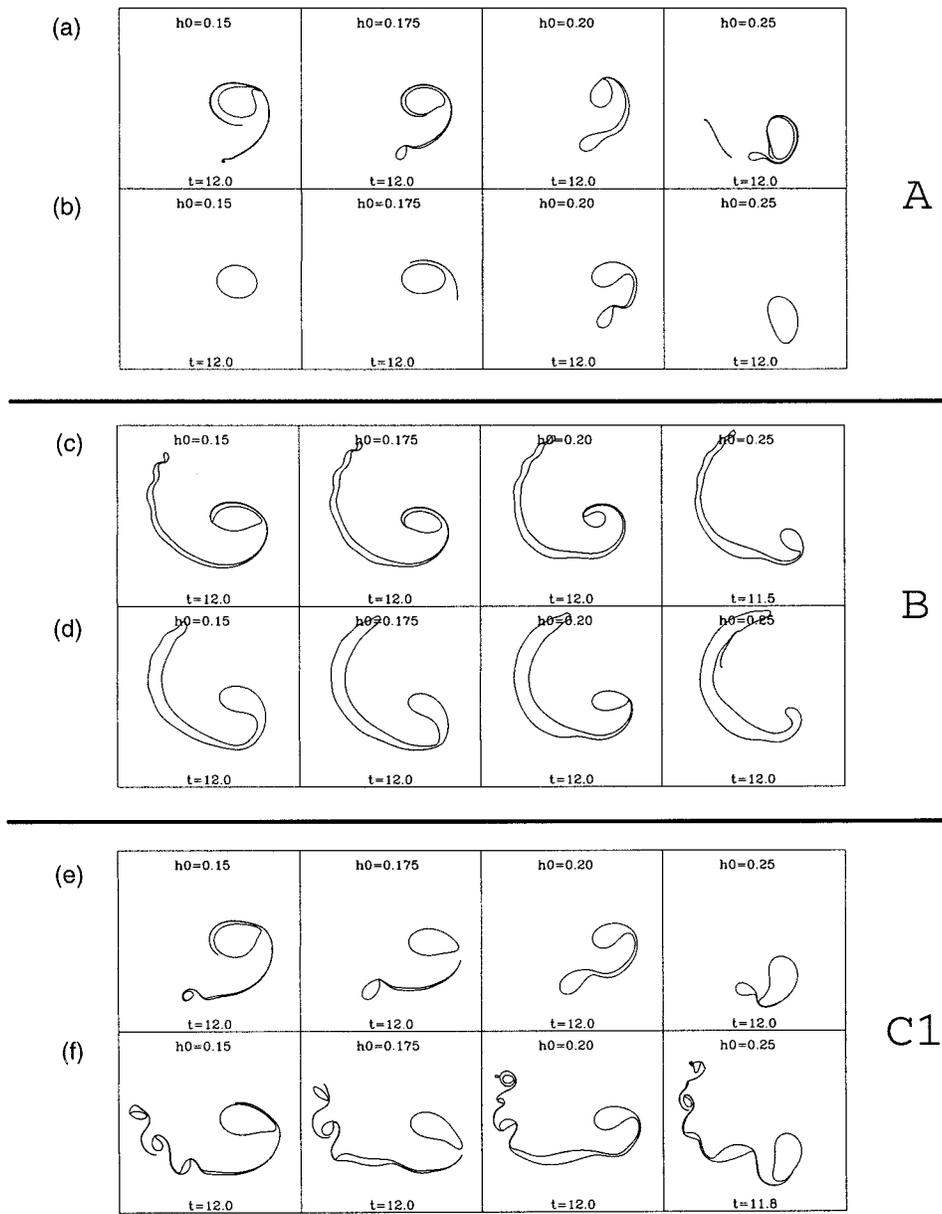Figures 6a and 6b show the PV in the upper layer at

FIG. 6. PV contours at $t = 12$ in upper layer (layer 10) with $h_0 = 0.15$, 0.175, 0.20, and 0.25 (left to right) for vortices (a) V2 and (b) V3 (family $\mathcal{A}$); (c) V4 and (d) V5 (family $\mathcal{B}$); and (e) V6 and (f) V7 (family $\mathcal{C}1$).

day 12 for two vortices from family $\mathcal{A}$, for the same values of h_0 as in Fig. 5. For both vortices the PV in the bottom layer is essentially the same as for the barotropic vortex (see Fig. 5b) and is not shown; this is also true for all other vortices considered. The lack of significant variation in the evolution in the lower layers for different initial vortices is related to the choice of initial vortices: all vortices have the same total circulation and, as shown in Figs. 1 and 2, have very similar, nearly barotropic structure in lower layers. There is, however, a dramatic difference in the evolution in the upper layers for different values of $\hat{q}_1$. For small $\hat{q}_1$ there

is always wave breaking at the top of the domain (for this range of h_0), but for $\hat{q}_1 \geq 0.1 f_0$ there is wave breaking in the upper layer only for an intermediate range of h_0. Note that there are large differences in the characteristics of the wave breaking even for values of $\hat{q}_1$ for which wave breaking always occurs in the upper layer; for example, compare Figs. 5a and 6a. The above simulations indicate that cylindrical vortices with PV increasing with height are more resilient than barotropic vortices.

The suppression of wave breaking in upper levels with increased $\hat{q}_1$ is consistent with the linear wave anal-
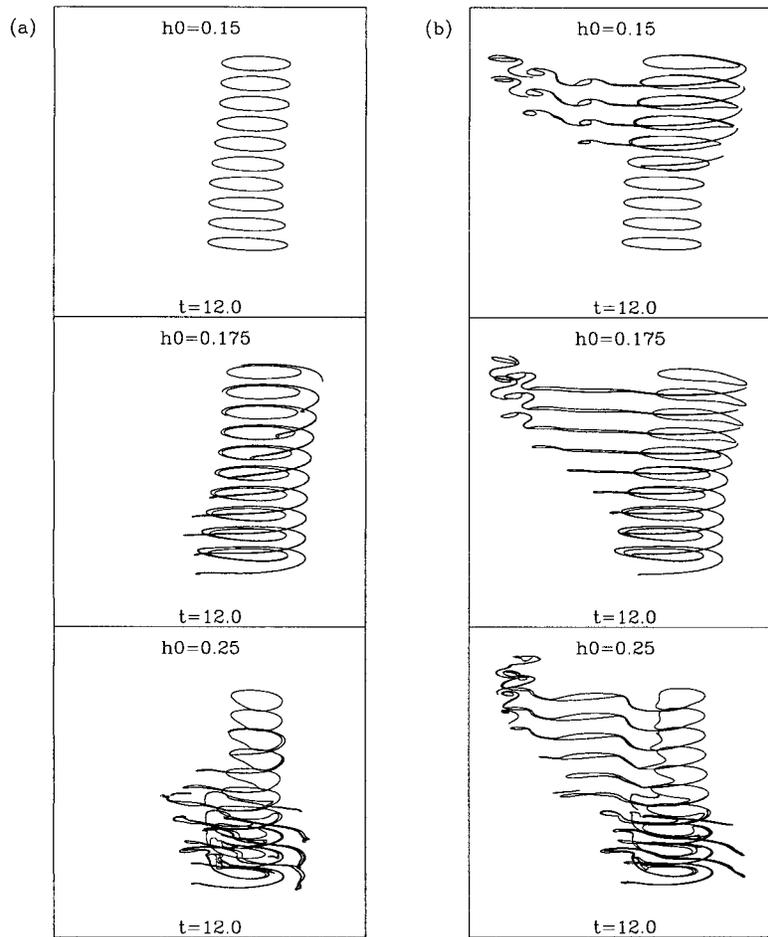
FIG. 7. Side view at $t = 12$ for vortices V3 (left) and V7 (right) with $h_0 = 0.15$, 0.175, and 0.25 (top to bottom).

ysis. As $\hat{q}_1$ increases (for constant A) the amplitude of linear waves in the upper layers reduces for fixed disturbance amplitude at the bottom of the vortex; see Fig. 4. This reduced disturbance amplitude then implies that the critical amplitude for the onset of wave breaking will increase with $\hat{q}_1$, consistent with the contour dynamics simulations.

Figures 6c and 6d show the PV in the upper layer for two vortices from family $\mathcal{B}$ (again the evolution in the bottom layer is very similar to Fig. 5b and is not shown). For both vortices (and for vortices with larger $\hat{A}_1$) the evolution in the upper layer is qualitatively the same as for the barotropic case; that is, wave breaking occurs throughout the range of h_0 considered. There are, however, quantitative differences; in particular, the width of the filaments in the upper layers increases with $\hat{A}_1$. However, these differences are much smaller than those for vortices within family $\mathcal{A}$, and broadly speaking the wave breaking at the edge of a vortex with constant PV is relatively insensitive to vertical variations in the area of the vortex.

The PV in the upper layer for two vortices from fam-

ily $\mathcal{C}1$ are shown in Figs. 6e and 6f. These plots should also be compared with Fig. 6b, which shows a third vortex from this family (see Fig. 2). Although the initial flows for these three vortices are very similar, there is a surprisingly large variation in the nonlinear evolution of the upper layers of the vortices. As the slope of the vortex edge with height increases (i.e., $\hat{A}_1$ increases), the amount of wave breaking in the upper layers increases. As discussed above, for a cylindrical vortex ($\hat{A}_1 = 0$) there is no wave breaking in the upper layers for small or large forcing amplitude. But for $\hat{A}_1 \geq 0.5\pi$ there is wave breaking in upper layers for all amplitudes shown, and there is breaking in lower layers for large amplitudes. Another noticeable difference for large $\hat{A}_1$ is that the filaments produced in the upper layers are unstable and roll up into small vortices; this is discussed further below. The dramatic changes in the evolution of the vortices within family $\mathcal{C}1$ are clearly shown in Fig. 7, which shows side views of vortices V3 and V7 for three different forcing amplitudes.

The simulations for vortices in family $\mathcal{C}1$ show that there can be a dramatic difference in the nonlinear evo-

lution of waves on the edge of a vortex for vortices with only small changes in $A(z)$. Note, however, that these dramatic changes do not occur for the same variations in $A(z)$ if q is independent of z, that is, family $\mathcal{B}$. Hence, the variation of the evolution of vortex-edge waves to variations in either q or A cannot be considered in isolation.

b. Vortex structure

We now examine in more detail the vertical structure and temporal evolution of the vortex "core." The vortex core is determined by applying the coarse-graining technique of Waugh (1992) (see also Polvani et al. 1995); that is, the surgery algorithm is applied to the results of the contour dynamics simulations with a sufficiently large surgery scale (δ) to disconnect filaments from the vortex core ($\delta = 0.1\hat{R}_b$, approximately 300 km, is used here). The structure of the vortex core is then quantified using the elliptical diagnostics (EDs) of Waugh (1997) (see also Legras and Dritschel 1993; Dritschel 1993). The EDs define the area (α), center (x_c, y_c), elongation (aspect ratio, λ), and orientation (θ) of the vortex in each layer. The EDs can be used not only to diagnose the variation of the vortex core for different initial vortices and forcing amplitudes, but also to compare the simulations with observed stratospheric polar vortices (e.g., Waugh and Randel 1999).

Figure 8 shows the temporal and vertical variation of the equivalent radius R_E (the radius of circle with same area as the contour, $R_E = \sqrt{\alpha/\pi}$), distance of center of vortex from the origin r_c, and aspect ratio λ of the vortex, for the barotropic vortex with $h_0 = 0.175$ (see Fig. 5 for plots of the vortex in the upper and lower layers at $t = 12$).

The vortex area R_E is constant until between days 8 and 9, at which time the area decreases suddenly. This sudden decrease is because the width of the filament being drawn from the vortex decreases below the surgery cutoff scale, and the surgery removes the filament from the vortex core. If a larger (smaller) cutoff value is used, this decrease in area occurs slightly later (earlier). The vortex erosion (decrease in area) occurs first in the lower layers, but the magnitude of the erosion is largest in the upper layers. Note that for $h_0 = 0.175$ the wave breaking is in the intermediate breaking regime where it occurs throughout the domain (see Fig. 5).

There is a large temporal variation in the distance of the vortex center from the origin, $r_c(z)$ (see Fig. 8b). There is a local maxima around days 3–5, with the maxima in the upper layer lagging that in the lower layer by around 1 day. During this period r_c increases with z (i.e., the vortex tilts equatorward with height). Between days 5 and 7 the vortex moves back toward the origin, and there is a local minima in r_c around day 7.5 (at which time the vortex is centered near the pole at all but the upper levels). Over the last part of the simulation
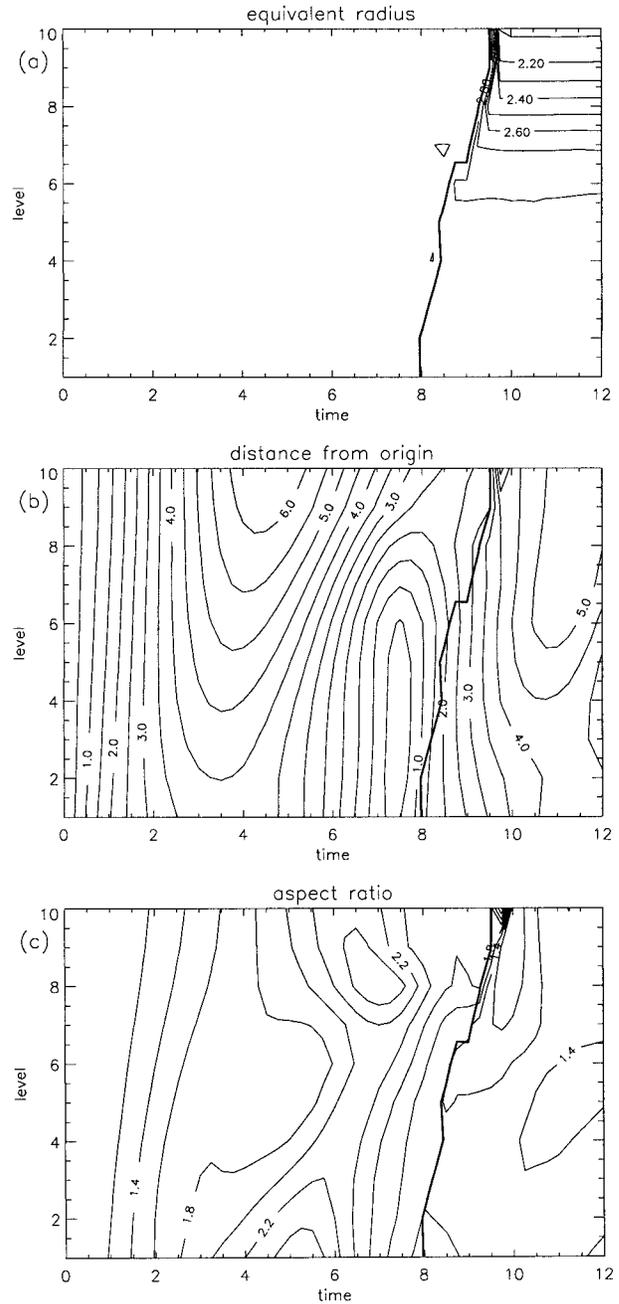

FIG. 8. Altitude–time contour plots of (a) R_E, (b) r_c, and (c) λ for vortex V1 with $h_0 = 0.175$.

(during which filaments are drawn from the vortex) the vortex moves away from the origin at all levels.

The elongation (aspect ratio λ) of the vortex increases during the first half of the simulation, and maximum elongation occurs between days 5 and 7 (with a time lag of around 2 days between the top and bottom layers). The maximum λ occurs after the maximum in r_c but around the same time as the onset of wave breaking, and is larger in the upper and lower layers than in the
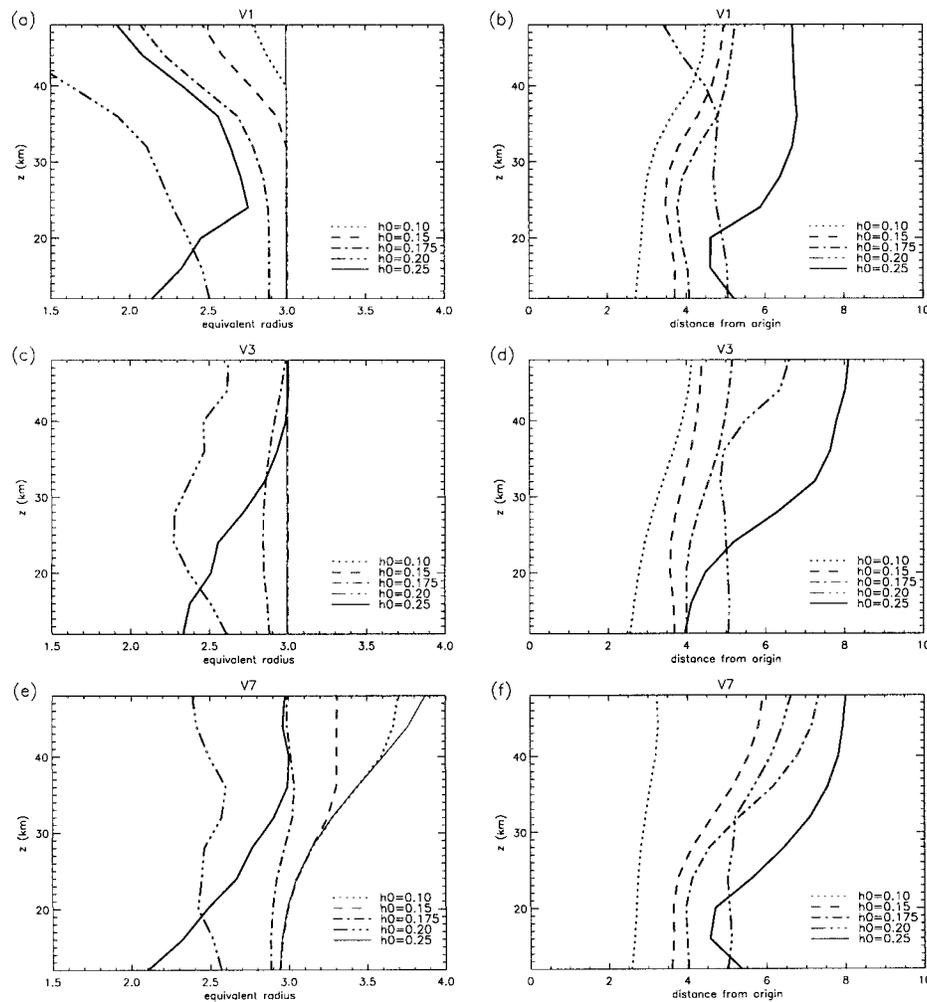
FIG. 9. Vertical variation of equivalent radius R_E and distance from origin r_c at $t = 12$ for vortices (a), (b) V1; (c), (d) V3; and (e), (f) V7; and several different values of h_0 (see legends). Thin solid curves show the initial values.

middle layers. Over the last few days of the simulation the vortex core is nearly circular at all levels. Note that as λ is calculated from spatial moments of the contour, the value of λ for an elongated vortex with a connected filament can be very different from that of the vortex core alone (Waugh 1997); hence, care should be taken when interpreting λ during the onset of wave breaking (before the surgery algorithm has removed any filaments from the vortex core).

The vertical and temporal variations of the vortex core structure varies with h_0 and between vortices. However, for a given vortex, the timing and vertical variation of the maxima and minima of r_c and the timing of the maxima in λ are qualitatively similar for all h_0, with the amplitude of the maxima increasing with h_0. Similarly, the decrease in R_E (i.e., vortex erosion) increases with h_0. The variations in $R_E(z)$ and $r_c(z)$ at day 12 with h_0 for three different initial vortices (V1, barotropic;

V3, R constant, q increasing with z; V7, R and q increasing with z) are shown in Fig. 9.

The variation of $R_E(z)$ clearly shows the differences in the vertical extent of the wave breaking (and subsequent vortex erosion). For vortices V1 and V7, R_E at $t = 12$ for weak forcing ($h_0 \leq 0.15$) is less than its original value only in the upper layers, and the smaller h_0, the more vertically confined the region where R_E differs from its original value; that is, erosion occurs only in the upper layers. However, wave breaking does not occur for vortex V3 when $h_0 \leq 0.15$ (see Figs. 6, 7) and there is no change in R_E for these values of h_0. For moderate forcing ($h_0 = 0.175$ to 0.20) there is wave breaking at all levels of the vortex for all vortices (see Fig. 6) and R_E is less than its original value for all z. For V1 and V7 the erosion is larger in the upper layers than in the bottom layers, but for V3 the erosion is largest in the middle of the vortex. For large forcing
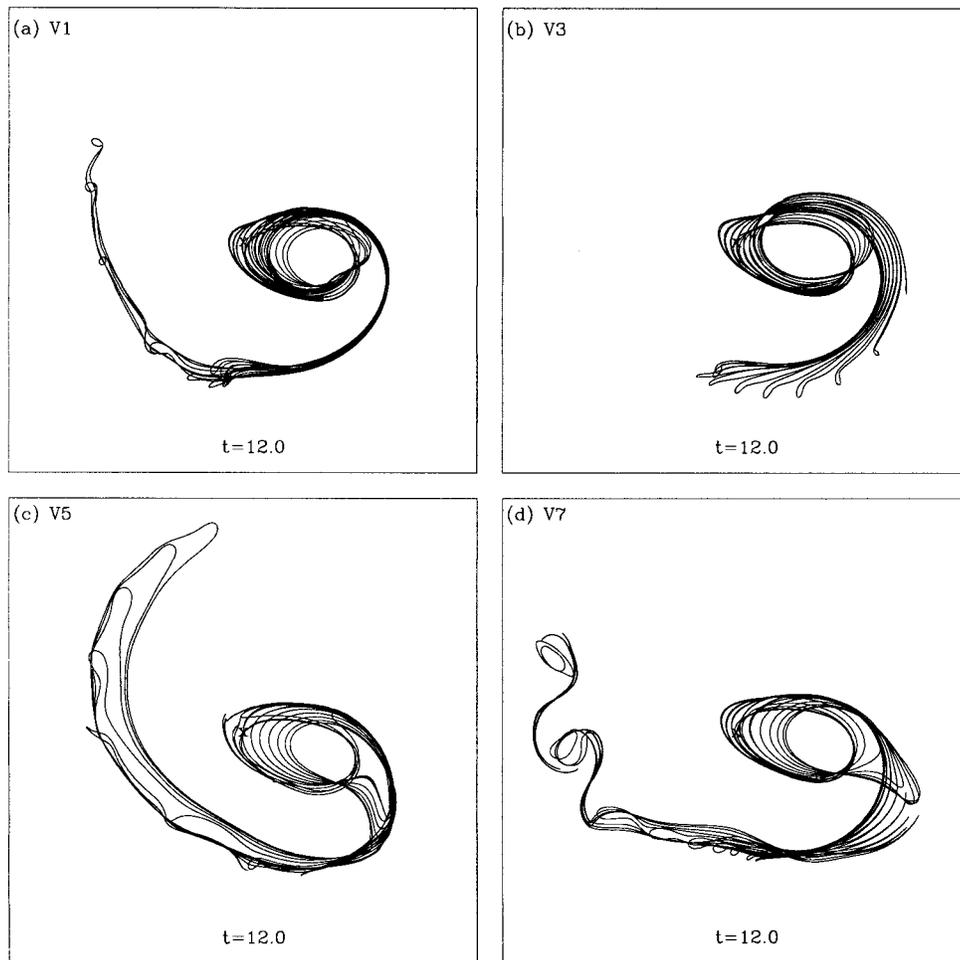
FIG. 10. PV contours in all 10 layers at $t = 12$ for vortices (a) V1, (b) V3, (c) V5, and (d) V7.

($h_0 = 0.25$) there is again erosion at all levels for vortices V1 and V7 with the largest erosion at the bottom and top of the vortex, but for V3 there is erosion only at the bottom of the vortex.

The erosion of vortex V7 for h_0 around 0.15 to 0.175 is intriguing. As shown in Fig. 9e, in this case the area at day 12 is roughly constant with height and hence the structure is very similar to that of vortex V3. As shown above there is very little erosion of V3 for these forcing amplitudes, and hence this raises the possibility that if the simulation for vortex V7 was continued a time may be reached where wave breaking (or vortex erosion) stops. However, as diabatic processes cannot be ignored over a longer timescale these processes need to be included if this is to be examined further.

The variation of r_c at day 12 with z and h_0 is similar for all vortices; see Fig. 9. In nearly all cases r_c increases with z, and both r_c at the bottom of the vortex and $\partial r_c / \partial z$ increase with h_0. In other words, the vortices tilt away from the origin with increasing height, and the distance from the origin and slope increases with forcing amplitude. Note that, as shown in Fig. 8, there is a strong

temporal variation in $r_c(z)$, and different results are obtained if the above comparison is made at a different time.

c. Filament structure

DS94 noted that the filaments in their simulations were vertically aligned. However, this alignment could be because they considered only initially barotropic vortices, and we now examine the slope of the filaments in simulations of baroclinic vortices. Note that Fig. 7 shows that the filaments have vertical coherence, and hence it is more appropriate [as discussed by Schoeberl and Newman (1995)] to refer to the filaments in each layer as a single sheet of PV. However, as the term "filament" is commonly used in the stratospheric dynamics literature we will continue to use this term when discussing the sheets of PV. (Furthermore, the term "vortex sheet" has a very different meaning in the vortex dynamics literature.)

Figure 10 shows the PV in all layers after 12 days for simulations with $h_0 = 0.175$ and for vortices V1,

V3, V5, and V7. This clearly shows that the characteristics of the filaments produced during wave breaking varies with the initial vortex structure. There is a significant slope to the filaments only for vortex V3, which has fixed radius and q increasing with z. Although the slope of filaments for vortex V5 (and to a much smaller degree, vortex V7) is sensitive to how the slope is defined, there is no slope in the outside edge of the filaments, but as the width of the filaments increases with height, the inside edge slopes poleward with height. The lack of significant slope for vortices V5 and V7 (and other vortices in families $\mathcal{B}$ and $\mathcal{C}$1) indicates that even when the edge of the initial vortex varies with height the filaments are generally vertically aligned. (Note that even for vortex V3 the slope of the filament is only 40:1, which is much smaller than the inverse Prandtl's ratio $N_0/f_0 \sim 200$.)

As noted earlier, for the vortices considered the location of the zero-wind line does not vary significantly with z (see Fig. 2). This raises the possibility that the absense of large vertical variations in the filament structure is because of the almost barotropic background flow away from the vortex in all cases considered. This issue will be examined in a future study that considers vortices with differing meridonal structure (and vertically varying zero-wind lines).

An interesting feature of the filaments produced in vortices with significant vertical variations in q and A is the roll-up of filaments. Filaments produced in barotropic simulations are usually stable and do not roll up into coherent vortices; this stability has been attributed to the strain/shear flow produced by the polar vortex (e.g., Dritschel 1989; Dritschel et al. 1991; Waugh and Dritschel 1991; Dritschel and Polvani 1992). The roll-up seen in the above simulations indicates that the flow surrounding baroclinic vortices may no longer suppress filament instability at upper levels. We are currently investigating whether this is because of the three-dimensional structure of the filaments or because of vertical variations in the (vortex induced) background strain/shear flow.

6. Discussion

Using a simple multilayer quasigeostrophic model we have examined the three-dimensional characteristics of wave propagation and breaking on the edge of polar vortices, and the dependence of these characteristics on the basic vortex structure.

The linear propagation of waves up the edge of a vortex is sensitive to vertical variations in the PV and in the area of the vortex. There is reduced wave propagation if the PV increases with height (while the area remains constant); this reduction becomes more pronounced with increasing disturbance wavenumber. For vortices with both PV and area varying with height, the variation in propagation is more complicated, but there is generally reduced propagation for greater variations in PV or area. This reduction in upward propagation of edge waves for baroclinic vortices implies that increased forcing amplitudes are required for wave breaking to occur.

The characteristics of the nonlinear evolution, in particular the wave breaking, are also sensitive to variations in the structure of the vortex. For vortices with PV increasing with height (with area constant), the wave breaking in the upper layers is much less than in the case of a barotropic vortex: there is no longer wave breaking for small amplitude forcing and the wave breaking is more vertically confined for large amplitude. When both the PV and area of the vortex increase with height, there is again wave breaking in upper layers for small and large amplitude forcing. However, there is a surprisingly large difference in the characteristics of the wave breaking for vortices with the same (vertically varying) velocity at the vortex edge but differing shape: not only does the vertical extent of the wave breaking vary, but so do the characteristics of the filaments produced by the wave breaking (when q and A both vary, the filaments in upper layers are unstable and roll up into a series of small vortices).

The simulations presented have shown that the characteristics of wave breaking at edge of vortex vary with the structure of the vortex, and that some vortex structures are more resilient than others (e.g., vortices with increasing PV are more resilient than barotropic vortices). This raises an interesting question; namely, does the polar vortex naturally develop in this way? That is, can the observed seasonal evolution of the vortex structure (see section 3) be related to this change in the characteristics of wave breaking? We may venture that the answer is yes, as one can argue that the shape and structure of the polar vortex are inherently connected with the mechanisms that force and dissipate it (e.g., Butchart and Remsburg 1986; O'Neill and Pope 1993; Peirce et al. 1993). However, the present model needs to be extended to include other processes, such as radiative effects, to fully address this question.

It will be of interest to see if the different characteristics of the wave breaking (e.g, roll-up of filaments and the vertical extent of wave breaking–vortex erosion) are observed to occur in the real stratosphere. One approach to examine this could be to perform multilayer high-resolution trajectory calculations (as in Schoeberl and Newman 1995) for different periods (when the vortex structure is different). Note that such calculations during January 1992 show some indication of filament roll-up in the middle and upper stratosphere [see, e.g., Fig. 15 of Waugh et al. (1994)]. Another approach could be to compare the elliptical diagnostics from the contour dynamics simulations with those derived from analyzed PV (Waugh and Randel 1999), particularly during periods when the observed vortex is highly distorted (e.g., stratospheric warmings).

The multilayer QG contour dynamics numerical model used in this study is computationally efficient [in fact,

the efficiency of contour dynamics calculations has increased dramatically with the development of the contour-advective semi-Lagrangian scheme (CASL) (Dritschel and Ambaum 1997), which is 1000 times faster than the standard contour dynamics method used here], and this enables a large area of parameter space to be covered. However, as there are several approximations in this model (e.g., piecewise constant PV and QG planar flow) it is not fully understood to what degree the results will carry over to the real stratosphere (or more realistic 3D models). But previous comparisons have shown excellent agreement between multicontour contour dynamics and pseudospectral calculations with a continuous PV distribution (e.g., Legras and Dritschel 1993; Waugh 1993), indicating that using piecewise constant PV does not significantly effect the results. Furthermore, there is good qualitative agreement between the results from the series of planar contour dynamics simulations of a forced vortex patch by Polvani and Plumb (1992) and those from the spherical pseudospectral simulations of a polar vortex with smoothly varying PV by Yoden and Ishioka (1993). These studies therefore indicate that valuable insight into the dynamics of polar vortices can be gained from planar models that represent the vortex by patches of constant PV. However, it should be noted that the above comparisons were for single-layer calculations, and it is not clear what effect the approximations used in this model have on the three-dimensional flow considered here. Support, though, for the results presented here can be seen in the recent simulations of L. M. Polvani and R. Saravanan (1998, personal communication): in simulations using a spherical, primitive equation, pseudospectral model they find roll-up of filaments in the upper levels for baroclinic vortices and reduced wave breaking for vortices with increased vertical shear.

In this study we have considered only vortices represented by a single contour in each layer. The new fast CASL code will enable multiple contours to be used in each layer, and an analysis of the sensitivity of the wave propagation and breaking characteristics to meridional PV gradients (and location of the zero-wind line). Also, we have examined the nonlinear response only for steady wavenumber-1 forcing: it would be interesting to examine the response to forcing with different spatial structure and/or temporal variation. For example, examining the response to a pulse of localized forcing might provide insight into the connection between tropospheric blocking events and stratospheric intrusion events (e.g., Plumb et al. 1994) or warming events (e.g., Quiroz 1986). Another area of interest is the interaction between the tropopause and the stratospheric polar vortex, particularly in the subvortex region (e.g., Holton et al. 1995). This interaction could be examined by including a freely evolving tropopause (as in Saravanan 1994), as well as a stratospheric polar vortex, in the model.

REFERENCES

Beck, A., 1996: The stability of the northern stratospheric winter polar vortex in dependence on the horizontal resolution in a global model. *Beitr. Phys. Atmos.,* **69,** 449–460.

Boville, B. A., 1995: Middle atmosphere version of the CCM2 (MACCM2): Annual cycle and interannual variability. *J. Geophys. Res.,* **100,** 9017–9039.

Butchart, N., and E. E. Remsberg, 1986: The area of the stratospheric polar vortex as a diagnostic for tracer transport on an isentropic surface. *J. Atmos. Sci.,* **43,** 1319–1339.

——, S. A. Clough, T. N. Palmer, and P. J. Trevelyan, 1982: Simulations of an observed stratospheric warming with quasigeostrophic refractive index as a model diagnostics. *Quart. J. Roy. Meteor. Soc.,* **108,** 475–502.

Dritschel, D. G., 1988: Nonlinear stability bounds for inviscid, two-dimensional, parallel or circular flows with monotonic vorticity, and analogous three-dimensional quasi-geostrophic flows. *J. Fluid Mech.,* **191,** 575–581.

——, 1989: On the stablization of a two-dimensional vortex strip by adverse shear. *J. Fluid Mech.,* **206,** 193–221.

——, 1993: A fast contour dynamics method for many-vortex calculations in two-dimensional flows. *Phys. Fluids,* **5A,** 173–186.

——, and L. M. Polvani, 1992: The roll-up of vorticity strips on the surface of a sphere. *J. Fluid Mech.,* **234,** 47–69.

——, and R. Saravanan, 1994: Three-dimensional quasi-geostrophic contour dynamics, with an application to stratospheric dynamics. *Quart. J. Roy. Meteor. Soc.,* **120,** 1267–1298.

——, and M. de la Torre Juárez, 1996: The instability and breakdown of tall columnar vortices in a quasi-geostrophic fluid. *J. Fluid Mech.,* **328,** 129–160.

——, and M. H. P. Ambaum, 1997: A contour-advective semi-Lagrangian numerical algorithm for simulating fine-scale conservative dynamical fields. *Quart. J. Roy. Meteor. Soc.,* **123,** 1097–1130.

——, P. H. Haynes, M. Juckes, and T. G. Shepherd, 1991: The stability of a two-dimensional vortex filament under uniform strain. *J. Fluid. Mech.,* **230,** 647–666.

Fyfe, J., and X. Wang, 1997: Upper-boundary effects in a contour dynamics/surgery model of the polar stratospheric vortex. *Atmos.–Ocean,* **35,** 189–207.

Haynes, P. H., 1990: High-resolution three-dimensional modelling of stratospheric flows: Quasi-2D turbulence dominated by a single vortex. *Topological Fluid Mechanics,* H. K. Moffatt and A. Tsinober, Eds., Cambridge University Press, 345–354.

——, and W. E. Ward, 1993: The effect of realistic radiative transfer on potential vorticity structures, including the influence of background shear and strain. *J. Atmos. Sci.,* **50,** 3431–3453.

——, and J. Anglade, 1997: The vertical-scale cascade in atmospheric tracers due to large-scale differential advection. *J. Atmos. Sci.,* **54,** 1121–1135.

Holton, J. R., P. H. Haynes, M. E. McIntyre, A. R. Douglass, R. B. Rood, and L. Pfister, 1995: Stratosphere–troposphere exchange. *Rev. Geophys.,* **33** (4), 403–439.

Juckes, M. N., 1989: A shallow water model of the winter stratosphere. *J. Atmos. Sci.,* **46,** 2934–2954.

——, and M. E. McIntyre, 1987: A high-resolution one-layer model of breaking planetary waves in the stratosphere. *Nature,* **328,** 590–596.

Lahoz, W. A., and Coauthors, 1996: Vortex dynamics and the evo-

lution of water vapour in the stratosphere of the southern hemisphere. *Quart. J. Roy. Meteor. Soc.,* **122,** 423–450.

Legras, B., and D. G. Dritschel, 1993: A comparison of the contour surgery and pseudo-spectral methods. *J. Comput. Phys.,* **104,** 287–302.

Leovy, C. B., C.-R. Sun, M. H. Hitchman, E. E. Remsberg, J. M. Russell, L. L. Gordley, J. C. Gille, and L. V. Lyjak, 1985: Transport of ozone in the middle stratosphere: Evidence for planetary wave breaking. *J. Atmos. Sci.,* **42,** 230–244.

Mahlman, J. D., and L. J. Umscheid, 1987: Comprehensive modeling of the middle atmosphere: The influence of horizontal resolution. *Transport Processes in the Middle Atmosphere,* G. Visconti and R. R. Garcia, Eds., D. Reidel, 251–266.

Manney, G. L., J. D. Farrara, and C. R. Mechoso, 1994: Simulations of the February 1979 stratospheric sudden warming—Model comparisons and 3-dimensional evolution. *Mon. Wea. Rev.,* **122,** 1115–1140.

Mariotti, A., M. Moustaoui, B. Legras, and H. Teitelbaum, 1997: Comparison between vertical ozone soundings and reconstructed potential vorticity maps by contour advection with surgery. *J. Geophys. Res.,* **102,** 6131–6142.

McIntyre, M. E., 1992: Atmospheric dynamics: Some fundamentals, with observational implications. *Proc. Int. School Phys. "Enrico Fermi", CXV Course,* North-Holland, 313–386.

——, and T. N., Palmer, 1983: Breaking planetary waves in the stratosphere. *Nature,* **305,** 593–600.

——, and ——, 1984: The 'surf zone' in the stratosphere. *J. Atmos. Terr. Phys.,* **46,** 825–849.

Mechoso, C. R., 1990: The final warming of the stratosphere. *Dynamics, Transport and Photochemistry in the Middle Atmosphere of the Southern Hemisphere,* A. O'Neill, Ed., Kluwer 55–67.

Norton, W. A., 1994: Transport and stirring by breaking Rossby waves in a single layer model of the wintertime stratosphere. *J. Atmos. Sci.,* **51,** 654–673.

O'Neill, A., and V. D. Pope, 1988: Simulations of linear and nonlinear disturbances in the stratosphere. *Quart. J. Roy. Meteor. Soc.,* **114,** 1063–1110.

——, and ——, 1993: The coupling between radiation and dynamics in the stratosphere. *Adv. Space Res.,* **13,** 351–358.

Orsolini, Y. J., 1995: On the formation of ozone laminae at the edge of the Arctic polar vortex. *Quart. J. Roy. Meteor. Soc.,* **121,** 1923–1941.

——, G. Hansen, U.-P. Hoppe, G. L. Manney, and K. H. Fricke, 1997: Dynamical modelling of wintertime lidar observations in the Arctic: Ozone laminae and ozone depletion. *Quart. J. Roy. Meteor. Soc.,* **123,** 785–800.

Pierce, B. R., W. T. Blackshear, T. D. Fairlie, W. L. Grose, and R. E. Turner, 1993: The interaction of radiative and dynamical processes during a simulated stratospheric warming. *J. Atmos. Sci.,* **50,** 3829–3851.

Plumb, R. A., and Coauthors, 1994: Intrusions into the lower strato-

spheric Arctic vortex during the winter of 1991/92. *J. Geophys. Res.,* **99,** 1089–1106.

Polvani, L. M., and R. A. Plumb, 1992: Rossby wave breaking, filamentation and secondary vortex formation: The dynamics of a perturbed vortex. *J. Atmos. Sci.,* **49,** 462–476.

——, D. W. Waugh, and R. A. Plumb, 1995: On the subtropical edge of the stratospheric surf zone. *J. Atmos. Sci.,* **52,** 1288–1309.

Quiroz, R., 1986: The association of stratospheric warmings with tropospheric blocking. *J. Geophys. Res.,* **91,** 5277–5285.

Randel, W. J., 1992: Global atmospheric circulation statistics, 1000–1 mb. NCAR Tech. Note NCAR/TN-366+STR, 256 pp.

Rose, K., 1985: Rossby waves in a 3-D numerical model for sudden stratospheric warmings. *Beitr. Phys. Atmos.,* **58,** 220–236.

Salby, M. L., D. O'Sullivan, R. R Garcia, and P. Callaghan, 1990a: Air motion accompanying the development of a planetary wave critical layer. *J. Atmos. Sci.,* **47,** 179–203.

——, R. R Garcia, D. O'Sullivan, and P. Callaghan, 1990b: The interaction of horizontal eddy transport and thermal drive in the stratosphere. *J. Atmos. Sci.,* **47,** 1647–1665.

——, ——, ——, and J. Tribbia, 1990c: Global transport calculations with an equivalent barotropic system. *J. Atmos. Sci.,* **47,** 188–214.

Saravanan, R., 1994: Modelling the tropopause–surface interactions: A contour dynamics approach. *Proc. Int. Symp. on the Life Cycles of Extratropical Cyclones,* Vol. 2, Bergen, Norway, 511–516.

Schoeberl, M. R., and D. L. Hartmann, 1991: The dynamics of the stratospheric polar vortex and its relation to springtime ozone depletions. *Science,* **251,** 46–52.

——, and P. A. Newman, 1995: A multiple-level trajectory analysis of vortex filaments. *J. Geophys. Res.,* **100,** 25 801–25 815.

Waugh, D. W., 1992: The efficiency of symmetric vortex merger. *Phys. Fluids,* **4A,** 1745–1758.

——, 1993: Contour surgery simulations of a forced polar vortex. *J. Atmos. Sci.,* **50,** 714–730.

——, 1997: Elliptical diagnostics of stratospheric polar vortices. *Quart. J. Roy. Meteor. Soc.,* **123,** 1725–1748.

——, and D. G. Dritschel, 1991: The stability of filamentary vorticity in two-dimensional geophysical vortex-dynamics models. *J. Fluid Mech.,* **231,** 575–598.

——, and W. J. Randel, 1999: Climatology of Arctic and Antarctic polar vortices using elliptical diagnostics. *J. Atmos. Sci.,* **56,** 1594–1613.

——, and Coauthors, 1994: Transport of material out of the stratospheric Arctic vortex by Rossby wave breaking. *J. Geophys. Res.,* **99,** 1071–1088.

——, and Coauthors, 1997: Mixing of polar vortex air into middle latitudes as revealed by tracer-tracer scatter plots. *J. Geophys. Res.,* **102,** 13 119–13 134.

Yoden, S., and K. Ishioka, 1993: A numerical experiment on the breakdown of a polar vortex due to forced Rossby waves. *J. Meteor. Soc. Japan,* **71,** 59–72.